Manipulation and Certification of High-Dimensional Entanglement through a Scattering Medium

Baptiste Courme,[1] Patrick Cameron,[2] Daniele Faccio,[2] Sylvain Gigan⊙,[1] and Hugo Defienne⊙[2,3,*]

[1] *Laboratoire Kastler Brossel, École normale supérieure (ENS) − Université Paris Sciences & Lettres (PSL), CNRS, Sorbonne Université, Collège de France, 24 rue Lhomond, Paris 75005, France*

[2] *School of Physics and Astronomy, University of Glasgow, G12 8QQ Glasgow, United Kingdom*

[3] *Sorbonne Université, CNRS, Institut des NanoSciences de Paris (INSP), Paris F-75005, France*

High-dimensional entangled quantum states improve the performance of quantum technologies compared to qubit-based approaches. In particular, they enable quantum communications with higher information capacities or enhanced imaging protocols. However, the presence of optical disorder such as atmospheric turbulence or biological tissue perturbs quantum state propagation and hinders their practical use. Here, we demonstrate a wavefront shaping approach to transmit high-dimensional spatially entangled photon pairs through scattering media. Using a transmission matrix approach, we perform wave-front correction in the classical domain using an intense classical beam as a beacon to compensate for the disturbances suffered by a copropagating beam of entangled photons. Through violation of an Einstein-Podolski-Rosen criterion by 988σ, we show the presence of entanglement after the medium. Furthermore, we certify an entanglement dimensionality of 17. This work paves the way toward manipulation and transport of entanglement through scattering media, with potential applications in quantum microscopy and quantum key distribution.

I. INTRODUCTION

Quantum entanglement plays a central role in quantum technologies. In this respect, high-dimensional entangled states of light offer higher information capacities [1] and better resistance to noise [2] over qubit-based quantum communication systems. In particular, their high tolerance to losses makes them good candidates for the realization of device-independent quantum communication [3]. Furthermore, they also serve as an essential resource in many quantum imaging protocols, including sub-shot-noise imaging [4], resolution and sensitivity-enhanced approaches [5–8], quantum illumination [9,10], and quantum holography [11,12].

An important issue to be overcome in these applications is the preservation of entanglement after transmission through optical disorder. Light scattering in biological tissue, atmospheric turbulence, and random mode mixing in multimode fibers are examples of adverse effects that can significantly impair the performance of imaging and communication systems. In classical optics, wavefront shaping techniques [13,14] have been developed to mitigate these effects. Such an ability to control light propagation through scattering samples has led to many technological advances, such as the transmission of spatial information through multimode fibers [15,16] or deep tissue imaging [17,18].

Wavefront shaping has also been used to manipulate nonclassical light through scattering media, such as single [19–21] and indistinguishable photons [22,23]. These techniques have recently been applied to high-dimensional spatially entangled photon pairs. Proof-of-principle experiments include their transmission through thin static [24,25] and dynamic diffusers [26] and multimode fibers [27]. However, these demonstrations have several limits. In Refs. [24–26], the authors have demonstrated only the recovery of spatial correlations after the medium by performing measurements in a single spatial basis but not entanglement itself. In Ref. [27], entanglement has been certified at the output up to six dimensions. However, the proposed method works exclusively if the output state is characterized through a series of single-outcome spatial-mode measurements. In such a case, the number of measurements scales as $2d^2$, where d is the local dimension of the system, which leads to very long acquisition times

that are often prohibitive for real-world applications. More importantly, single-outcome measurement schemes use the assumption that the total number of coincidences in all modes does not fluctuate from one single-outcome measurement to the next, which is wrong in general [28]. Such an assumption would not be acceptable in an adversarial scenario such as quantum key distribution, as it would compromise the security of the protocol.

Here, we demonstrate the transport of high-dimensional entanglement through a scattering medium using a transmission matrix based wavefront shaping approach and a multi-outcome spatial measurement method. The transmission matrix of the scattering medium is first measured using classical light [14]. Then, a spatial light modulator (SLM) is programmed with a correction phase mask to mitigate scattering of entangled photons. Photon-correlation measurements in position and momentum are performed at the output using a commercially available single-photon avalanche diode (SPAD) camera [29]. The presence of entanglement after the medium is demonstrated through violation of an Einstein-Podolski-Rosen (EPR) criterion [30,31] with a confidence of 988σ. From our measurements in the position and momentum bases, we finally certify high-dimensional entanglement in up to 17 dimensions, using the method developed by Bavaresco *et al.* [32].

II. EXPERIMENTAL SETUP

Spatially entangled photon pairs are produced via spontaneous parametric down-conversion (SPDC) in a thin β-barium borate (BBO) crystal using the apparatus shown in Fig. 1(a). Two $4f$ imaging systems conjugate the output surface of the crystal onto a SLM and then onto a scattering medium. The scattering medium is a stretched layer of parafilm, placed on a microscope slide. At the output, photon pairs are detected using a commercial SPAD camera [33]. To measure momentum correlations, we use the lens f_7, positioned in a $2f$ arrangement to image the Fourier plane of the scattering layer onto the camera. To measure position correlations, lens f_5 is inserted to form a $4f$ arrangement and image the output surface of the scattering layer onto the camera. These two optical configurations allow measurements to be made in both the position and momentum bases, which form two mutually unbiased bases [34]. In the same apparatus, light emitted by a superluminescent diode (SLED) is collimated and superimposed onto the pump-beam propagation axis. This classical source is used to measure the transmission matrix T of the scattering medium, employing the method developed by Popoff *et al.* [14]. T is measured between 32×32 macropixels of the SLM (input-mode basis) and 192×192 pixels of a CCD camera (output-mode basis) positioned in a Fourier plane of the medium. Figure 1(b) shows the
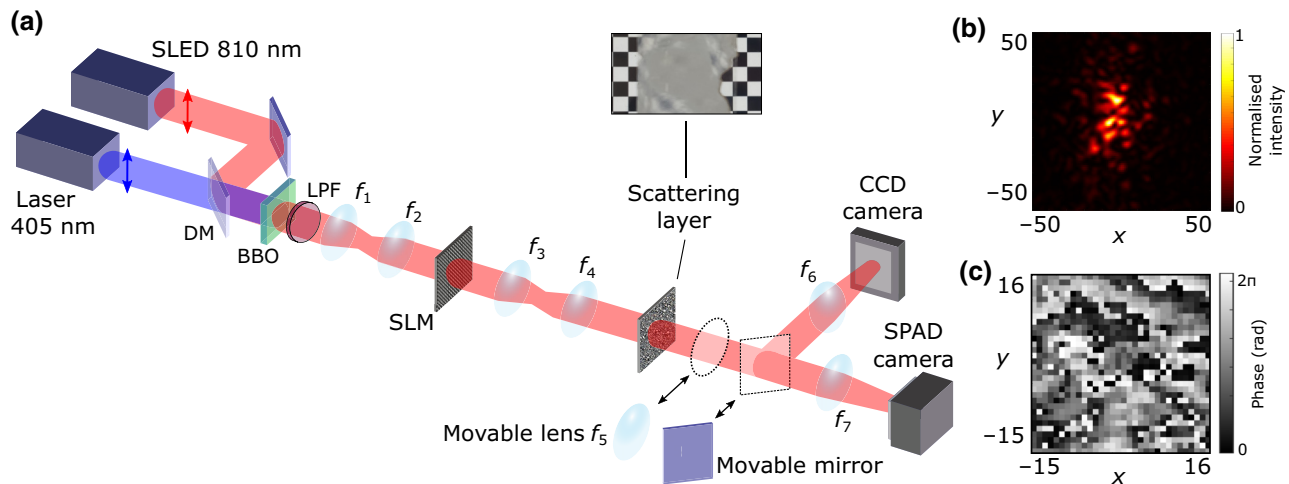

FIG. 1. The experimental setup. (a) Spatially entangled photon pairs are produced by type-I spontaneous parametric down-conversion (SPDC) by illuminating a β-barium borate (BBO) crystal (0.5-mm thickness) with a vertically polarized collimated laser diode (405 nm). Simultaneously, horizontally polarized and collimated light emitted by a superluminescent diode (SLED) is aligned along the pump beam using a dichroic mirror (DM). Long-pass and band-pass filters at 810 ± 5 nm (LPF) remove pump photons and filter the classical light. A two-lens system f_1-f_2 images the crystal surface onto a spatial light modulator (SLM), which is itself imaged by f_3-f_4 onto a scattering medium (a layer of parafilm on a microscope slide). In the momentum-basis configuration, a single-lens Fourier imaging system (f_6 or f_7) is used to image output light either onto a single-photon avalanche diode (SPAD) camera (with the movable mirror) or onto a charge-coupled device (CCD) camera (without the movable mirror). In the position-basis configuration, a movable lens f_5 is inserted to image the scattering layer onto the cameras. (b) An intensity image acquired by the CCD camera using classical light and no SLM correction. (c) The correction SLM pattern calculated using the transmission matrix. Note that the SLM is represented in transmission while it operates in reflection. The spatial units are in pixels.

intensity speckle pattern measured by the CCD with no phase pattern programmed on the SLM.

Using the transmission matrix formalism, the propagation of spatially entangled photon pairs in our optical system is written as

$$\Psi^{\text{out}} = TD\Psi^{\text{in}}D^t T^t, \tag{1}$$

where Ψ^{in} and Ψ^{out} are the spatial two-photon wave functions written in the discrete input and output basis, respectively, and D is a diagonal matrix associated with the SLM. D contains 1024 complex phase terms $\{e^{i\theta_k}\}_{k\in[\![1,1024]\!]}$, where θ_k is the phase term associated with the kth SLM macropixel. At this point, it is important to clarify the different mode bases under consideration. At the input, the basis is a position basis, where each mode corresponds to a SLM macropixel. In our experiment, since the SLM macropixels are much wider (120 μm) than the position correlation width of entangled photons in the SLM plane (24 μm), the input two-photon wave function can be approximated as $\Psi^{\text{in}} \approx \mathbb{1}$ (see Appendix G). At the output, the basis can be a position or a momentum basis according to the chosen configuration [Fig. 1(a)], where each mode corresponds to a camera pixel. When measuring the transmission matrix, the camera is positioned in a Fourier plane of the system, which means that the output basis is a momentum basis. To switch to a position basis, we insert the lens f_5 in the system and substitute $T \to FT$ in Eq. (1), where F is a matrix associated with a discrete Fourier transform (see Appendix G).

To recover entanglement after the medium, one can program the SLM to restore spatial correlations between photon pairs simultaneously in the position and momentum bases, as would be the case without a scattering medium [29]. In other words, we are looking for a set of phases $\{\theta_k\}_{k\in[\![1,1024]\!]}$ so that D maximizes the following conditions:

$$|TD^2T^t|^2 = \mathbb{1}, \tag{2}$$

$$|FTD^2T^tF^t|^2 = \mathbb{1}. \tag{3}$$

In general, these conditions are difficult to satisfy by shaping the light with a single SLM. In our experiment, however, they can be simplified. First, since the scattering medium is a thin parafilm layer, the term FT is quasidiagonal, thus satisfying the condition given in Eq. (3). Second, we show in our simulations that the set of phases $\theta_k = \arg(T_{pk}^*)$, where p is an index associated with the central pixel of the CCD camera, is a solution that partially satisfies the condition given in Eq. (2) (see Appendix H). Figure 1(c) shows the corresponding SLM phase pattern. Note that this solution is the same as the one used to refocus classical light through the medium on the central camera pixel [14], through phase conjugation.

III. VIOLATION OF AN EPR CRITERION

We demonstrate the presence of spatial entanglement at the output by violating a separability criterion derived by Giovanetti *et al.* [31]. It states that separable systems satisfy the joint uncertainty product:

$$\Delta\mathbf{r}\Delta\mathbf{k} > \frac{1}{2}, \tag{4}$$

where the uncertainties $\Delta\mathbf{r} = \Delta(\mathbf{r_1} - \mathbf{r_2})$ and $\Delta\mathbf{k} = \Delta(\mathbf{k_1} + \mathbf{k_2})$ correspond to measures of the correlation widths associated with the joint probability distributions (JPDs) of photon pairs measured in position and momentum, respectively, for pairs of photons labeled 1 and 2. This criterion is commonly used to demonstrate the presence of entanglement in bipartite quantum systems [35–38]. To estimate $\Delta\mathbf{r}$ and $\Delta\mathbf{k}$, we measure the spatial JPD of photon pairs using the SPAD camera in the two configurations described in Fig. 1 [29,39]. In the momentum-basis
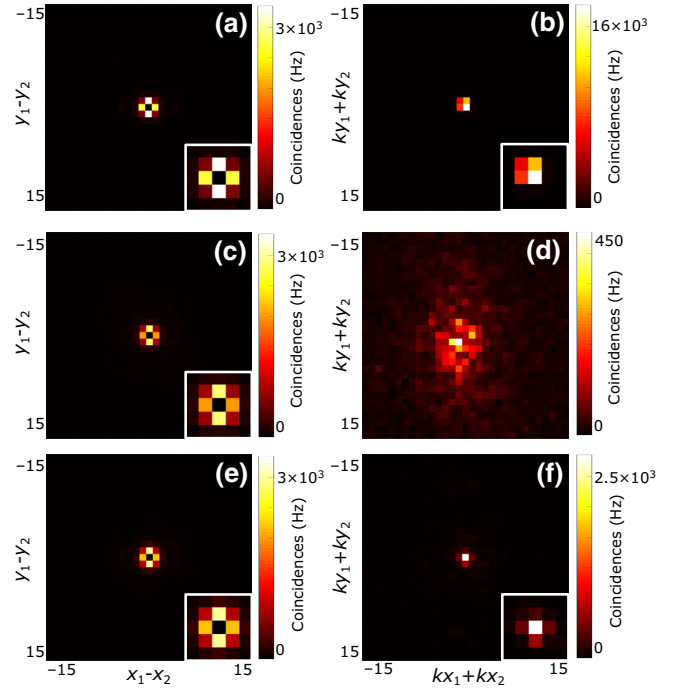

FIG. 2. Violation of the EPR criterion. Images of JPD minus-coordinate projections acquired using the position-basis configuration (a) without the scattering medium, (c) with the medium and no SLM correction, and (e) with the medium and SLM correction. Images of JPD sum-coordinate projections acquired using the momentum-basis configuration (b) without the scattering medium, (d) with the medium and no SLM correction, and (f) with the medium and SLM correction. Analysis is performed on a total of 1.5×10^9 images. The central pixel in the minus-coordinate projections is set to zero because the SPAD camera does not resolve the number of photons and therefore cannot measure photon coincidences at the same pixel. The spatial units are in pixels.

configuration, the width of the central peak in the JPD sum-coordinate projection corresponds to $\Delta\mathbf{k}$. Accounting for the effective magnification of our optical system, we measure $\Delta\mathbf{k} = 1.495(1) \times 10^4$ m^{-1} without the scattering medium [Fig. 2(a)] and $\Delta\mathbf{k} = 1.72(1) \times 10^4$ m^{-1} with the scattering medium and SLM correction [Fig. 2(e)]. The width values are estimated using a Gaussian model [40] (see Appendix D). In the presence of the medium but without SLM correction, the spatial correlations become spread and distorted [Fig. 2(c)], making it difficult to properly estimate $\Delta\mathbf{k}$. As discussed in Ref. [41], an approximate value can nevertheless be obtained by measuring the width of the envelope $\Delta\mathbf{k} = 9.8(1) \times 10^4$ m^{-1}.

We repeat the above analysis in the position-basis configuration to extract $\Delta\mathbf{r}$. The projections of the JPD along the minus coordinate are measured without the medium [Fig. 3(b)], with the medium and no SLM correction [Fig. 3(d)], and with the medium and SLM correction [Fig. 3(f)]. In all cases, a coincidence peak is observed at the center of the projection that demonstrates strong position correlations between photon pairs. Accounting for the optical magnification, we measure $\Delta\mathbf{r} = 6.77(1) \times 10^{-6}$ m (no medium), $\Delta\mathbf{r} = 8.32(2) \times 10^{-6}$ m (medium and no SLM correction), and $\Delta\mathbf{r} = 8.82(2) \times 10^{-6}$ m (medium and SLM correction) by fitting with a Gaussian (see Appendix D). The measured values of the transverse position and momentum correlation widths violate the separability criterion $\Delta\mathbf{r}\Delta\mathbf{k} = 0.1013(1) < 1/2$ without the medium and $\Delta\mathbf{r}\Delta\mathbf{k} = 0.1519(2) < 1/2$ with the

medium and SLM correction, thus demonstrating the presence of spatial entanglement. The confidence levels are $C = 2589$ and $C = 988$, respectively (see Appendix E). In the presence of the medium and without SLM correction, a similar calculation shows that $\Delta\mathbf{r}\Delta\mathbf{k} = 0.82(1) > 1/2$, with a confidence level of $C = 41$, and we conclude that the separability criterion is not violated. However, this last calculation must be interpreted with caution, because our measurement of the width of the envelope in Fig. 2(d) to evaluate $\Delta\mathbf{k}$ is only approximate, as the latter does not necessarily follow a Gaussian shape. The impossibility of detecting the presence of entanglement in this case is confirmed properly using the certification method in Sec. IV.

IV. CERTIFICATION OF HIGH-DIMENSIONAL ENTANGLEMENT

Measurements in two mutually unbiased bases (MUBs) enable the use of a recently developed entanglement witness for certifying high-dimensional entanglement [32]. The discrete position and momentum bases can be used as two MUBs and are accessible in our experimental setup [34]. As shown in Figs. 3(a) and 3(e), we select $d = 45$ pixels uniformly distributed over a central region in both configurations. Modes associated with the chosen pixels are denoted $\{|m\rangle\}_{m \in [\![0,d-1]\!]}$ (discrete position basis) and $\{|\widetilde{p}\rangle\}_{p \in [\![0,d-1]\!]}$ (discrete momentum basis). To certify entanglement dimensionality of the detected
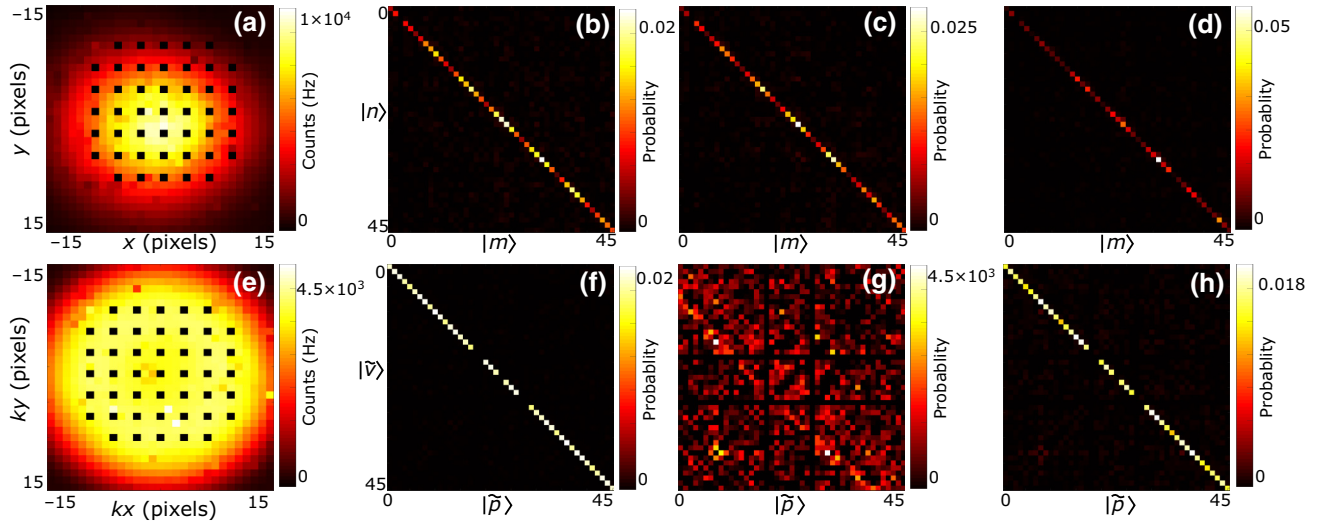

FIG. 3. Entanglement certification. (a) An intensity image acquired in the position-basis configuration, showing the grid of 45 pixels. (b)–(d) Correlation matrices between all the pixels in the grid of the position basis (b) without the medium, (c) with the medium and a flat SLM, and (d) with the medium and a correction SLM. Each pixel is labeling the spatial coordinates of the photon: $|m\rangle$ in the position basis. (e) An intensity image acquired in the momentum-basis configuration, showing the grid of 45 pixels. (f)–(h) Correlation matrices between all the pixels in the grid in the momentum basis (f) without the medium, (g) with the medium and a flat SLM, and (h) with the medium and a correction SLM. Each pixel is labeling the spatial coordinates of the photon: $|\widetilde{p}\rangle$ in the momentum basis. Analysis is performed on a total of 1.5×10^9 images. The black lines and columns are associated with hot pixels of the sensor being set to zero.

state ρ, correlation measurements are performed in the two MUBs to compute a lower bound for the fidelity of the state with respect to a maximally entangled target state $|\Psi\rangle = 1/\sqrt{d} \sum_{m=0}^{d-1} |mm\rangle$. Without the scattering medium, we obtain a lower-bound value of the fidelity $\widetilde{F}(\rho, \Psi) = 0.6138$ from the correlation matrices measured in Figs. 3(b) and 3(f). The entanglement dimensionality that is certifiable with this method is the maximal r such that

$$r < \widetilde{F}(\rho, \Psi)\, d + 1. \tag{5}$$

In our experiment, this allows us to certify the presence of 28 dimensions of entanglement without the medium. In the presence of the scattering medium and no SLM correction, we obtain a negative lower-bound value of the fidelity from the correlation matrices measured in Figs. 3(c) and 3(f) and no entanglement can be certified. After applying the SLM correction, strong correlations in position and momentum are again measurable [Figs. 3(d) and 3(g)] leading to a lower-bound value of the fidelity of $\widetilde{F}(\rho, \Psi) = 0.37$ that allows us to certify 17 dimensions of entanglement (see Appendix F).

In practice, the number of dimensions certified at the output depends on our ability to compensate for scattering but also on the total acquisition time, i.e., the number of frames used to compute the correlation matrices [29]. In order to isolate the role played by wavefront shaping itself, Fig. 4 analyzes the number of certified dimensions as a function of the number of frames. While it always remains zero with a scattering medium and no correction (green curve), it increases until it reaches a plateau at around 1.2 billion frames in the case without the medium (blue curve) and with the medium and SLM correction (red curve). The existence of such plateaus is predicted in our simulations (see Appendix H). Because they do not depend on the acquisition time, the values of these plateaus are therefore
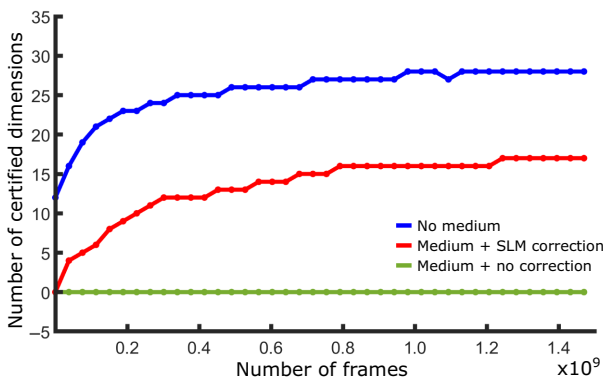

FIG. 4. The certified-dimension analysis. The number of certified dimensions for different total numbers of frames without the medium (blue curve), with the medium and SLM correction (red curve), and with the medium and no correction (green curve).

the relevant quantities to compare in order to evaluate the performance of wavefront shaping for transporting entanglement. In our experiment, we quantify a 39% loss in the number of dimensions. Such a decrease is due to optical losses (i.e., modes not collected at the output) and to the inability, for a single SLM, to perfectly correct a scattering medium such as parafilm which, although relatively thin, is not a simple random phase mask.

V. DISCUSSION AND CONCLUSIONS

In summary, we show the transport of high-dimensional spatial entanglement through a scattering medium using a transmission matrix based wavefront shaping technique. Using a multi-outcome spatial measurement approach with a SPAD camera, we demonstrate violation of the EPR criterion with a confidence of 988σ and certify 17 dimensions of entanglement at the output of the medium. Although our demonstration uses a rather thin scattering medium, the matrix approach [Eq. (1)] that we introduce can be used with any linear scattering medium. In practice, however, the use of thicker scattering media would spread the correlations over many more spatial modes, many of which would not be collected, making the experiment very challenging [42]. Furthermore, finding a solution that satisfies both the conditions given in Eqs. (2) and (3) to certify the entanglement at the output is not obvious in the general case, especially when using a single SLM to shape light. The use of multiplane light-conversion technologies [43–46], together with more sensitive and faster single-photon cameras such as the next-generation SPADs [47] or fast time-stamping cameras [48], could be promising solutions to advance these issues. Simulations provided in Appendix H confirm the potential of multiplane light conversion. Finally, one advantage of our approach is the use of an intense classical light beam to characterize and correct scattering, before switching to the quantum source. This approach could also enable similar approaches in dynamic media, such as biological tissues and atmospheric turbulent layers, which brings us closer to real-world applications.

B.C. performed the experiment. B.C., P.C., and H.D. analyzed the results. H.D. conceived the original ideal,

designed the experiment, and supervised the project. All authors discussed the data and contributed to the manuscript.

APPENDIX A: DETAILS ON THE EXPERIMENTAL APPARATUS

The pump is a collimated continuous-wave laser at 405 nm (Coherent OBIS-LX) with an output power of 100 mW and a beam diameter of 0.8 ± 0.1 mm. The SLED is centered at 810 nm and has a total bandwidth of approximately 20 nm (Superlum). The BBO crystal has dimensions $0.5 \times 5 \times 5$ mm and is cut for type-I SPDC at 405 nm with a half opening angle of 3 degrees (Newlight Photonics). The crystal is slightly rotated around the horizontal axis to ensure near-collinear phase matching of photons at the output (i.e., a ring collapsed into a disk). A 650-nm-cutoff long-pass filter is used to block pump photons after the crystals, together with a band-pass filter centered at 810 ± 5 nm. The SLM has 1080×1920 pixels with a pitch of 8 μm and uses a liquid crystal on silicon technology (Holoeye model Pluto-NIR-II). The SPAD camera is the model SPC3 from Micron Photon Devices. It has 32×64 pixels, a pixel pitch of 45 μm, and is operated in the free-running mode with an exposure time of 1 μs. The $4f$ imaging system, f_1-f_2, in Fig. 1(a) is represented by two lenses for clarity but is in reality composed of a series of four lenses with focal lengths 50 mm, 150 mm, 100 mm, and 200 mm, respectively. The first and the last lens are positioned at focal distances from the crystal and the SLM, respectively, and the distance between two lenses in a row equals the sum of their focal lengths. Similarly, the second $4f$ imaging system, f_3-f_4, in Fig. 1(a) is composed of a series of four consecutive lenses with focal lengths 200 mm, 100 mm, 75 mm, and 50 mm, respectively, arranged as in the previous case. The other lenses have the following focal lengths: $f_5 = 30$ mm, $f_6 = 100$ mm, and $f_7 = 150$ mm. In the momentum-basis configuration, the system effective focal length is 75 mm. In the position-basis configuration, the imaging-system magnification is $\times 10$.

APPENDIX B: JPD MEASUREMENT AND PROJECTIONS

In the experiments shown in our work, the measured JPD Γ takes the form of a four-dimensional matrix containing $(N_Y \times N_X)^4$ elements, where $N_Y = 32$ and $N_X = 64$ correspond to the size of the sensor. An element of the matrix is written Γ_{ijkl}, where (i, j) and (k, l) are pixel labels corresponding to spatial positions (x_i, y_j) and (x_k, y_l). It is measured by acquiring a set of $M + 1$ frames $\{I^{(l)}\}_{l \in [\![1,M+1]\!]}$ using a fixed exposure time and then processing them using

the formula [29,39]:

$$\Gamma_{ijkl} = \frac{1}{M} \sum_{l=1}^{M} \left[I_{ij}^{(l)} I_{kl}^{(l)} - I_{ij}^{(l)} I_{kl}^{(l+1)} \right]. \tag{B1}$$

Because the SPAD camera does not resolve the number of photons, photon coincidences at the same pixel (i.e., coefficients Γ_{ijij}) cannot be measured and are therefore set to zero. In addition, note that correlation values between neighboring pixels suffer from crosstalk and must be corrected (see Appendix C).

Γ_{ijkl} is a discrete version of the continuous JPD $\Gamma(\mathbf{r_1}, \mathbf{r_2}) = |\psi(\mathbf{r_1}, \mathbf{r_2})|^2$, where ψ is the spatial two-photon wave function associated with photon pairs and $\mathbf{r_1} = x_1 \mathbf{e_x} + y_1 \mathbf{e_y}$ and $\mathbf{r_2} = x_2 \mathbf{e_x} + y_2 \mathbf{e_y}$ are transverse spatial positions ($\mathbf{e_x}$ and $\mathbf{e_y}$ are unit vectors along the x and y axes, respectively). Such a continuous formalism is used in many theoretical works describing the propagation of spatially entangled photon pairs [40,49]. In our work, to measure the correlations strength in position and momentum, one must project the JPD along the sum and minus coordinates (Fig. 2). The sum-coordinate P^+ and minus-coordinate P^- projections are defined as follows:

(1) Using the continuous formalism, the sum-coordinate projection P^+ is defined as

$$P^+(\mathbf{r^+}) = \int \Gamma(\mathbf{r}, \mathbf{r^+} - \mathbf{r}) d\mathbf{r}. \tag{B2}$$

where $\mathbf{r} = x\mathbf{e_x} + y\mathbf{e_y}$. It represents the probability of detecting pairs of photons generated in all symmetric directions relative to the position $\mathbf{r^+} = x^+ \mathbf{e_x} + y^+ \mathbf{e_y}$. In practice, it is calculated using the discrete-space formula

$$P_{i^+ j^+}^+ = \sum_{i=1}^{N_X} \sum_{j=1}^{N_Y} \Gamma_{(i^+ - i)\ (j^+ - j)\ i\ j}. \tag{B3}$$

(2) Using the continuous formalism, the minus-coordinate projection P^- is defined as

$$P^-(\mathbf{r^-}) = \int \Gamma(\mathbf{r}, \mathbf{r^-} + \mathbf{r}) d\mathbf{r}. \tag{B4}$$

where $\mathbf{r} = x\mathbf{e_x} + y\mathbf{e_y}$. This represents the probability of two photons of a pair being detected in coincidence between pairs of pixels separated by an oriented distance $\mathbf{r^-} = x^- \mathbf{e_x} + y^- \mathbf{e_y}$. In practice, it is calculated using the discrete-space formula

$$P_{i^- j^-}^- = \sum_{i=1}^{N_X} \sum_{j=1}^{N_Y} \Gamma_{(i^- + i)\ (j^- + j)\ i\ j}. \tag{B5}$$

APPENDIX C: CROSSTALK CORRECTION AND HOT-PIXEL IDENTIFICATION

The design of the architecture of SPAD cameras involuntarily leads to an undesirable detection event when a photon or a dark count triggers a pixel [50]. As a detection event is created by a charge avalanche due to the first triggering, an electron can reach a neighboring pixel and trigger it, leading to a crosstalk event. In our work, the average crosstalk probability distribution is first characterized by performing long measurements with the shutter closed (i.e., where only dark counts, evenly distributed over the sensor, trigger the pixels) and then removed from the collected data. Furthermore, our SPAD detector exhibits some defective pixels with a higher than normal detection rate [51]. As a result, they lead to multiple fake-detection events. In our work, we first identify these hot pixels by performing a long measurement with no light on the sensor and applying a threshold to the resulting image. The values of these pixels are then set to zero in all subsequent acquisitions. More details about crosstalk and hot-pixel removal processes are provided in the following.

1. Crosstalk correction process

Our SPAD camera has some crosstalk issues due to the design of the sensor. As a result, each term of the JPD Γ_{ijkl} can be decomposed into two contributions:

$$\Gamma_{ijkl}^{(\text{raw})} = \Gamma_{ijkl}^{(\text{opt})} + \Gamma_{ijkl}^{(\text{ct})}, \qquad (\text{C1})$$

where $\Gamma_{ijkl}^{(\text{opt})}$ is the contribution originating from photon coincidence between pixels (i,j) and (k,l) and $\Gamma_{ijkl}^{(\text{ct})}$ is the contribution originating from crosstalk events between the same pixels. Figure 5 shows the intensity of the crosstalk between two pixels of the sensor as a function of the distance between them. It is obtained by measuring the JPD with no light on the sensor (noted Γ_{ijkl}^{0}) and projecting it along the minus coordinate. As expected, the crosstalk is nonzero only between pixel pairs that are close to each
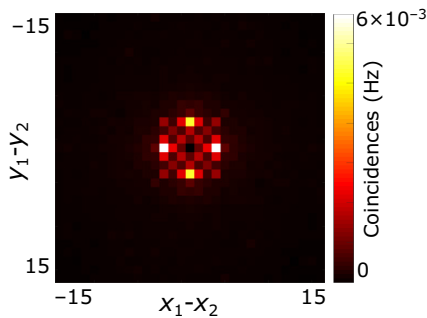
other, mostly between pixels less than 3 pixels apart (in both directions).

In addition to having a specific shape, crosstalk correlations also depend on the intensity detected on each of the pixels concerned. In short, the more photons are detected by a pair of pixels, the more crosstalk coincidence events are produced. As a result, if the intensity is nonuniform, the crosstalk is spatially dependent. To remove the crosstalk correlations from the measured JPD, we use a correction model that takes into account the intensity dependence:

$$\Gamma_{ijkl} = \Gamma_{ijkl}^{(\text{raw})} - \Gamma_{ijkl}^{0}\alpha_{kl}\sqrt{I_{ij}}, \qquad (\text{C2})$$

where I_{kl} is the intensity at pixel (k,l) and α_{kl} is a correction parameter. In a previous work [52], crosstalk correction has been achieved by setting the parameters $\alpha_{kl} = \alpha\sqrt{I_{kl}}$, where α is a constant. However, the SPAD camera was a different model than ours. In our case, we observe that α cannot be set to a constant to correct the crosstalk properly over all the pixels. The reason is probably that the crosstalk pattern shown in Fig. 5 is in reality nonuniform across the sensor. To take this effect into account, the parameters α_{kl} are set using the formula

$$\alpha_{kl} = \frac{\Gamma_{ijk(l-3)}^{(\text{raw})} + \Gamma_{ijk(l+3)}^{(\text{raw})}}{\Gamma_{ijk(l-3)}^{0} + \Gamma_{ijk(l+3)}^{0}}. \qquad (\text{C3})$$

Here, we use the fact that the photon-pair correlation width in the camera plane is much smaller than 135 μm = 3 pixels. This means in practice that correlation values between pixels separated by ±3 pixels are only due to crosstalk, i.e., $\Gamma_{ijk(l\pm3)}^{(\text{raw})} = \Gamma_{ijk(l\pm3)}^{(\text{ct})}$. In Eq. (C3), we use these values as reference values to adapt the weight of the correction term $\Gamma_{ijkl}^{0}\sqrt{I_{ij}}$, which enables us to compensate for the nonuniformity of the crosstalk shape. Figures 6(a)–6(d) show conditional probability images before ($\Gamma_{ijkl}^{(\text{raw})}$) and after ($\Gamma_{ijkl}$) crosstalk correction.

2. Hot-pixel identification process

To remove the hot pixels, we first acquire 1.2×10^9 frames with no light on the sensor and sum them to obtain the intensity image shown in Fig. 7. We then apply a threshold to the image: all pixels with a value above 10% of the maximum are identified as hot pixels and set to zero in all further acquisitions. In total, 32 pixels out of a total of 2048 are identified.

APPENDIX D: GAUSSIAN MODEL OF THE TWO-PHOTON WAVE FUNCTION

The two-photon wave function $\psi(\mathbf{r_1}, \mathbf{r_2})$ associated with photon pairs produced by type-I SPDC at the surface of a thin nonlinear crystal can be approximated using a
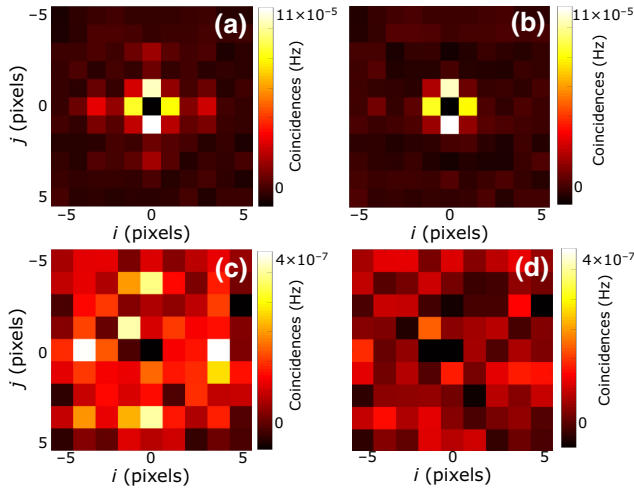

FIG. 5. The crosstalk intensity pattern. The JPD minus-coordinate projection measured with no light falling on the sensor. A total of 7×10^8 frames are acquired.

FIG. 6. Conditional probability images before and after crosstalk removal. (a) $\Gamma_{ijkl}^{(raw)}$ and (b) Γ_{ijkl} acquired in the position-basis configuration without the medium. The reference pixel (k, l) is the central pixel $(0, 0)$. (c) $\Gamma_{ijkl}^{(raw)}$ and (d) Γ_{ijkl} acquired in the position momentum-basis configuration without the medium. The reference pixel (k, l) is the central pixel $(0, 0)$. A total of 7×10^8 frames are acquired.

Gaussian model [40,49]:

$$\psi(\mathbf{r_1}, \mathbf{r_2}) = A \, \exp\left(\frac{-|\mathbf{r_1} - \mathbf{r_2}|^2}{4\sigma_\mathbf{r}^2}\right) \exp\left(\frac{-|\mathbf{r_1} + \mathbf{r_2}|^2 \sigma_\mathbf{k}^2}{4}\right),$$
(D1)

where $\sigma_\mathbf{r}$ and $\sigma_\mathbf{k}$ are the position and momentum correlation widths of the photons at the output of the
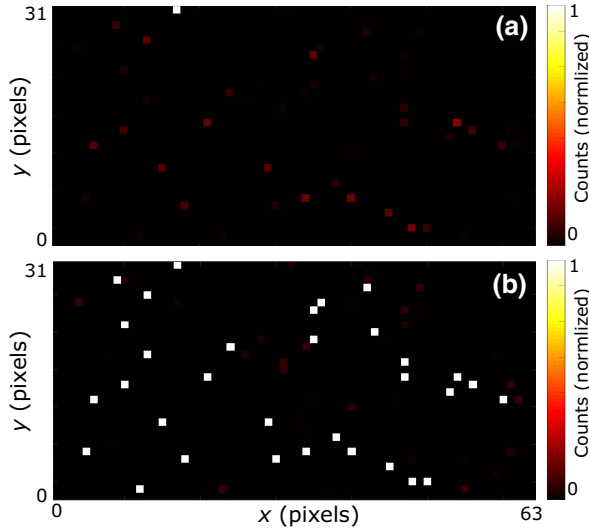

FIG. 7. The identification of hot pixels. (a) An intensity image obtained by summing 1.2×10^9 frames acquired with no light on the sensor. (b) The same image with the 32 identified hot pixels appearing in white.

crystal, respectively, and A is a constant. As a result, minus- and sum-coordinate JPD projections measured in the position and momentum basis, respectively, also have Gaussian shapes, i.e., $\exp(-|\mathbf{r_1} - \mathbf{r_2}|^2/2\sigma_\mathbf{r}^2)$ and $\exp(-|\mathbf{k_1} + \mathbf{k_2}|^2/2\sigma_\mathbf{k}^2)$. Under this approximation, the correlation widths $\sigma_\mathbf{r}$ and $\sigma_\mathbf{k}$ are exactly identified with the uncertainties $\Delta \mathbf{r} = \Delta(\mathbf{r_1} - \mathbf{r_2})$ and $\Delta \mathbf{k} = \Delta(\mathbf{k_1} + \mathbf{k_2})$ [31, 35]. This justifies the use of a Gaussian model to extract the values of $\Delta \mathbf{r}$ and $\Delta \mathbf{k}$, as shown in Fig. 2. However, it should be kept in mind that if the two-photon wave function can no longer be modeled by a Gaussian, as is the case with the medium and no SLM correction [Fig. 2(d)], then the correspondence with $\Delta \mathbf{r}$ and $\Delta \mathbf{k}$ values is no longer exact. This issue would also occur in the case of thicker scattering media, as we expect the SLM to refocus coincidences in the central peak but with a nonzero coincidence background surrounding it.

APPENDIX E: CONFIDENCE LEVEL ON VIOLATION OF THE EPR CRITERION

Equation (1) shows the EPR separability criterion considered in our work [31]. This criterion has been used in previous works to demonstrate the presence of entanglement between photons with different types of detectors, including scanning single-pixel detectors [35], the scientific CMOS (sCMOS) camera [38], the electron-multiplying CCD (EMCCD) camera [36,37], and the SPAD camera [29]. To achieve violation of the EPR criterion, transverse position and momentum correlation widths, $\Delta \mathbf{r}$ and $\Delta \mathbf{k}$, are first estimated by fitting the sum- and minus-coordinate projections of the momentum- and position-basis configurations by a Gaussian model [36,37,40] of the form $f(r) = a \exp(-r^2/2\Delta^2)$, where a is a fitting parameter and Δ is the desired correlation-width value $\Delta \mathbf{r}$ or $\Delta \mathbf{k}$ (for more details about the Gaussian model, see Appendix D). The presence of noise in the sum- and minus-coordinate images induces uncertainties with regard to the values $\Delta \mathbf{r}$ and $\Delta \mathbf{k}$ returned by the fitting process. The standard deviation of the noise Σ is measured in an area composed of 15×15 pixels surrounding the central coincidence peak. The link between the correlation-width uncertainty δ_Δ ($\delta_\Delta = \delta_{\Delta \mathbf{r}}$ or $\delta_{\Delta \mathbf{k}}$) and Σ is given by calculating the value of $grad[f]$ at the position $r = \Delta$: $|df/dr(r = \Delta)| = a/(\Delta\sqrt{e})$. Then, expanding it at the first order in r, $\delta f = a\delta r/(\Delta\sqrt{e})$. In our case, the variations δf and δr are identified with the uncertainty quantities Σ and δ_Δ, respectively, which finally leads to

$$\delta_\Delta = \frac{\Sigma\sqrt{e}\Delta}{a}.$$
(E1)

All correlation-width values and uncertainties are expressed in the coordinate system of the crystal, after taking into consideration the magnifications introduced by the

imaging systems detailed in Fig. 1(a). Then, the confidence level of the EPR violation is defined as

$$C = \frac{|1/2 - \Delta\mathbf{r} \cdot \Delta\mathbf{k}|}{\sigma}, \qquad \text{(E2)}$$

where $\sigma = \Delta\mathbf{r} \cdot \Delta\mathbf{k}\sqrt{(\delta_{\Delta\mathbf{k}}/\Delta\mathbf{k})^2 + (\delta_{\Delta\mathbf{r}}/\Delta\mathbf{r})^2}$ is the uncertainty of the product $\Delta\mathbf{r} \cdot \Delta\mathbf{k}$. The confidence level essentially expresses the deviation of the measured value $\Delta\mathbf{r}\Delta\mathbf{k}$ from the violation limit. Its unit is a number of σ.

APPENDIX F: ENTANGLEMENT CERTIFICATION

In our experiment, we use discrete transverse position and momentum bases given by a set of pixels defined on the SPAD camera and denoted as $\{|m\rangle\}_{m\in[\![1;d]\!]}$ and $\{|\tilde{p}\rangle\}_{p\in[\![1;d]\!]}$, respectively. Our approach is based on the protocol proposed by Erker *et al.* [34], where these bases are used as two MUBs) to certify high-dimensional entanglement. They are linked according to

$$|\tilde{p}\rangle = \frac{1}{\sqrt{d}} \sum_{m=0}^{d-1} \omega^{km} |m\rangle, \qquad \text{(F1)}$$

where $\omega = e^{2\pi i/d}$. Experimentally, these bases are accessed using lenses to image or Fourier image the output of the nonlinear crystal. A subset of pixels is then selected in the illuminated areas of the sensor to optimize the coincidence signals measured. In our case, we select 45 pixels evenly separated from each other by 2 pixels and located on a disk. One difference between the scheme of Erker *et al.* [34] and our work is that only one image is produced on the camera in our case, compared to two in their proposal using a beam splitter. Our setup prevents us from accessing the coincidence rate at the same pixel, i.e., the same spatial mode. Instead, the coincidence rate of photon pairs in the same pixel is inferred by measuring the coincidence rate between each pixel and its neighbor. This inference leads to a lower value of the intrapixel coincidence rate in the position basis, which therefore underestimates the real entanglement-witness value.

To certify the presence of high-dimensional entanglement in the measured state ρ, we employ a recently developed witness that uses correlations in at two MUBs [32], i.e., $\{|m\rangle\}_{m\in[\![1;d]\!]}$ and $\{|\tilde{p}\rangle\}_{p\in[\![1;d]\!]}$. Using coincidence measurements in these two bases, one can determine a lower bound for the fidelity $F(\rho, \Phi)$ of the state ρ to a pure bipartite maximally entangled target state $|\Phi\rangle$. Since the fidelity to a target entangled state also provides information about the dimensionality of entanglement, we use this bound for certifying the dimension of entanglement of the state produced in our experiment. We consider a maximally entangled target state written as

$$|\Phi\rangle = \frac{1}{\sqrt{d}} \sum_{m=0}^{d-1} |mm\rangle, \qquad \text{(F2)}$$

with $d = 45$. The fidelity $F(\rho, \Phi)$ of the state ρ to the target state $|\Phi\rangle$ is defined as

$$\begin{aligned} F(\rho, \Phi) &= \mathrm{Tr}\,(|\Phi\rangle\langle\Phi|\rho) \\ &= \sum_{m,n=0}^{d-1} \langle mm|\rho|nn\rangle \\ &= F_1(\rho, \Phi) + F_2(\rho, \Phi), \end{aligned} \qquad \text{(F3)}$$

where

$$F_1(\rho, \Phi) = \sum_{m=0}^{d-1} \langle mm|\rho|mm\rangle, \qquad \text{(F4)}$$

$$F_2(\rho, \Phi) = \sum_{m\neq n}^{d-1} \langle mm|\rho|nn\rangle. \qquad \text{(F5)}$$

The entanglement dimensionality can be deduced from the fidelity taking into account that for any state ρ of Schmidt number $r \leq d$, the fidelity of Eq. (F3) is bound by

$$F(\rho, \Phi) \leq B_r(\Phi) = \frac{r}{d}. \qquad \text{(F6)}$$

Hence, any state with $F(\rho, \Phi) > B_r(\Phi)$ must have an entanglement dimensionality of at least $r + 1$. Our goal is therefore to obtain a lower bound on the fidelity as large as possible for the target state the Schmidt rank of which is as close as possible to the local dimension d. To achieve this experimentally, the method described in Ref. [32] works by means of the following steps:

(1) Matrix elements $\{\langle mn|\rho|mn\rangle\}_{m,n}$ are calculated from the coincidence counts $\{N_{mn}\}_{mn}$ measured in the discrete position basis via

$$\langle mn|\rho|mn\rangle = \frac{N_{mn}}{\sum_{k,l} N_{kl}}. \qquad \text{(F7)}$$

These elements are shown in the matrix in Figs. 3(a)–3(c). They enable to calculate directly the term $F_1(\rho, \Phi)$ from the definition given by Eq. (F4).

(2) Matrix elements $\{\langle \tilde{p}\tilde{v}|\rho|\tilde{p}\tilde{v}\rangle\}_{pv}$ are calculated from the coincidence counts $\{\tilde{N}_{pv}\}_{pv}$ measured in the discrete momentum basis via

$$\langle \tilde{p}\tilde{v}|\rho|\tilde{p}\tilde{v}\rangle = \frac{\tilde{N}_{pv}}{\sum_{k,l} \tilde{N}_{kl}}. \qquad \text{(F8)}$$

These elements are shown in the matrices in Figs. 3(d)–3(f). These matrix elements, together

with those of the discrete position basis, allow us to bound the fidelity term $F_2(\rho, \Phi)$. This lower bound $\tilde{F}_2(\rho, \Phi)$ is calculated via

$$\tilde{F}_2(\rho, \Phi) = \sum_{p=0}^{d-1} \langle \tilde{p}\tilde{p}|\rho|\tilde{p}\tilde{p}\rangle - \frac{1}{d}$$
$$- \sum_{\substack{m \neq n', m \neq n \\ n \neq n', n' \neq m'}} \gamma_{mnm'n'} \sqrt{\langle mn|\rho|mn\rangle \langle m'n'|\rho|m'n'\rangle},$$
(F9)

where the prefactor $\gamma_{mnm'n'}$ is given by

$$\gamma_{mnm'n'} = \begin{cases} 0, & \text{if } (m - m' - n + n') \bmod d \neq 0, \\ \frac{1}{d}, & \text{otherwise.} \end{cases}$$
(F10)

A derivation of Eq. (F9) can be found in the "Methods" section of Ref. [32].

(3) A lower bound on entanglement is calculated as $\tilde{F}(\rho, \Phi) = F_1(\rho, \Phi) + \tilde{F}_2(\rho, \Phi) \leq F(\rho, \Phi)$. This lower-bound value is finally compared with the certification bound $B_r(\Phi)$ as

$$B_r(\Phi) < \tilde{F}(\rho, \Phi) \leq B_{r+1}(\Phi),$$
(F11)

thus certifying entanglement in $r + 1$ dimensions.

Using this approach, we note that no assumptions are directly made about the underlying quantum state ρ. However, assumptions are made about our measurement process. Indeed, by using Eq. (B1) to measure the JPD of photon pairs, we effectively perform a subtraction of accidental counts. Correcting for accidental coincidence is acceptable in our experiment, since we trust our measurement devices and the final goal is only to assess the presence of entanglement and its dimension. However, such an assumption would not be acceptable in an adversarial scenario such as quantum key distribution, as it would be likely to compromise the security of the protocol.

In addition, the sets of pixels selected to form the discrete position and momentum bases [Figs. 3(a) and 3(b)] are not perfectly mutually unbiased. Indeed, one set is obtained from the other by applying a continuous Fourier transform to a discrete set of modes, which is formally different than using a discrete Fourier transform. In our experimental configuration, however, the deviation from perfect unbiasedness is very small. To quantify it, we use an unbiasedness quantifier E_n defined as [53]

$$E_n = \sum_{\tilde{v}=0}^{d-1} p_{\tilde{v}|n} \log_2(p_{\tilde{v}|n}),$$
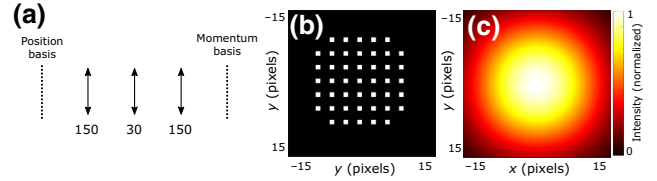(F12)

FIG. 8. The measurement of unbiasedness. (a) An experimental configuration representing the optical transformation that links the position and momentum bases in our experiment. (b) The spatial arrangement of the 45 selected pixels in the position and momentum optical planes. (c) The sinc-shaped intensity distribution produced by a pixel located in one optical plane into the reciprocal optical plane.

where $p_{\tilde{v}|n} = p_{\tilde{v}n}/\sum_{\tilde{v}} p_{\tilde{v}n}$, with $p_{\tilde{v}n} = |\langle \tilde{v}|\rho|n\rangle|^2$, $\{|n\rangle\}_{n \in [\![1;d]\!]}$ and $\{|\tilde{v}\rangle\}_{\tilde{v} \in [\![1;d]\!]}$ are the discrete transverse position and momentum bases and $d = 45$ is the dimension of the subspace. To estimate $p_{\tilde{v}n}$, we consider the optical configuration shown in Fig. 8(a). Such a configuration represents the effective optical transformation between the position and momentum bases in our experimental setup (Fig. 1). In practice, $p_{\tilde{v}n}$ can be seen as the intensity measured at the discrete position $|\tilde{v}\rangle$ in the momentum basis when a coherent source emits light from the position $|n\rangle$ in the position basis. In our experiment, values $p_{\tilde{v}n}$ can therefore be estimated from the spatial arrangement of all the pixels forming each basis and their shape. Figure 8(b) shows the spatial arrangement of the pixels in the two optical planes. It is the same in the momentum- and position-basis optical planes. In addition, each pixel is a square. The intensity produced by each pixel in the other basis therefore has the shape of a bidimensional sinc function and is independent of the pixel position. Figure 8(c) shows such an intensity distribution. Superimposition of Figs. 8(b) and 8(c) enables us to estimate the values $p_{\tilde{v}|n}$ for all $n \in [\![1;d]\!]$ and $\tilde{v} \in [\![1;d]\!]$. In our experiment, we then estimate $E_n = E = 5.479$. This value only differs by 0.5% from the maximum value of $\log_2(45) \approx 4.592$.

APPENDIX G: ENTANGLED-PHOTON MATRIX FORMALISM

Under the paraxial approximation, the propagation of spatially entangled photon pairs through a linear optical system is described using the formula [54]

$$\psi^{\text{out}}(\mathbf{r'_1}, \mathbf{r'_2}) = \iint h(\mathbf{r'_1}, \mathbf{r_1}) h(\mathbf{r'_2}, \mathbf{r_2}) \psi^{\text{in}}(\mathbf{r_1}, \mathbf{r_2}) d\mathbf{r_1} d\mathbf{r_2},$$
(G1)

where $h(\mathbf{r'}, \mathbf{r})$ is the impulse-response function of the linear system, $\psi^{\text{out}}(\mathbf{r'_1}, \mathbf{r'_2})$ and $\psi^{\text{in}}(\mathbf{r_1}, \mathbf{r_2})$ are the spatial two-photon wave functions in the output and input planes of the system, respectively, and $\{\mathbf{r_i}\}_{i=1,2}$ and $\{\mathbf{r_i'}\}_{i=1,2}$ are

the transverse spatial coordinates in the input and output planes, respectively. Using the same approach as for the propagation of coherent light [14], Eq. (G1) can be discretized into the following matrix form:

$$\Psi^{\text{out}} = H\Psi^{\text{in}}H^t, \qquad (\text{G2})$$

where H is the transfer matrix of the optical system, i.e., a discrete version of h, and Ψ^{out} and Ψ^{in} are matrices that represent discrete forms of the two-photon wave functions ψ^{out} and ψ^{in}, respectively. Note that, as in the classical matrix approach, the input and output planes are discretized as pixels (i.e., optical modes), which are then linearly ordered. This allows the use of matrices even if the associated functions h, ψ^{out}, and ψ^{in} are quadrivariate functions. In our experiment, $H = TD$, where T is the transmission matrix of the scattering medium and D is the diagonal matrix associated with the SLM. In our work, we also use the approximation $\psi^{\text{in}} \approx \mathbb{1}$ to obtain the conditions given in Eqs. (2) and (3). Indeed, photon pairs at the output surface of the crystal have strongly correlated transverse positions. We estimate the corresponding position correlation in the crystal plane to 4 μm using an EMCCD camera [36,37]. Accounting for the magnification between the crystal and the SLM, the correlation width in the SLM plane is about 24 μm, which is much smaller than the size of a macropixel used to measure the transmission matrix (120 μm). When discretized in the SLM macropixel basis, the matrix Ψ^{in} therefore has negligible off-diagonal components compared to its diagonal components, which allows us to approximate it to the identity matrix.

APPENDIX H: SIMULATIONS

Three types of simulations are conducted to support our experimental results. First, simulations based on matrix multiplications are used to predict Ψ^{out}. Equation (1) is computed using an experimentally measured transmission matrix, verifying that the correction SLM pattern [Fig. 1(c)] allows Ψ^{out} to satisfy the conditions in Eqs. (2) and (3). Second, simulations are performed in the general case of a thick scattering medium. They confirm the possibility of using our approach in this case and the interest in using multiplane light-conversion techniques. Third, simulations are performed to confirm the existence of a plateau at a large number of frames in the curves shown in Fig. 4. More details about these simulations are provided in the following.

1. Simulation of Ψ^{out} using the entangled-photon matrix approach

Figure 9 shows simulation results demonstrating the focusing of spatial correlations in the momentum basis through the scattering medium. The main steps of the
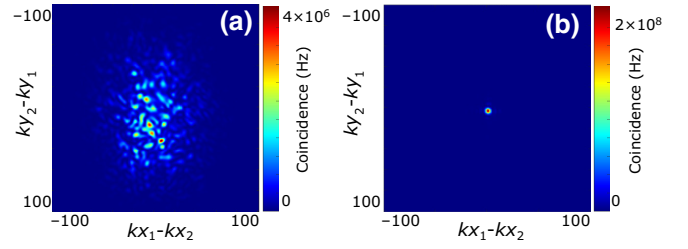

FIG. 9. Simulated two-photon output fields. Sum-coordinate projections of $|\Psi_{\text{out}}|^2$ obtained with (a) a flat phase pattern and the (b) correction phase pattern. The spatial coordinates are in pixels.

algorithm to obtain these results are described in the following:

(1) *Two-photon input field.* Exploiting the fact that in our experiment the correlation width of photon pairs in the SLM plane (24 μm) is much smaller than the size of a macropixel of the SLM (120 μm), the input two-photon wave function written in the SLM macropixel basis is approximated by an identity matrix. In MATLAB, it takes the form of a 1024 × 1024 identity matrix denoted as Ψ_{in}.

(2) *Propagation.* The two-photon field after propagation through the medium is obtained using the following equation:

$$\Psi_{\text{out}} = TD\Psi_{\text{in}}(TD)^T, \qquad (\text{H1})$$

where Ψ_{out} is the matrix associated with the two-photon output field, T is the transmission matrix of the system, and D is the diagonal matrix associated with the SLM. T is measured to be between 32 × 32 = 1024 macropixels of the SLM and 100 × 100 pixels of the CCD camera. Since we experimentally measure it using a copropagating reference, the transmission matrix obtained differs slightly from the real transmission matrix T, i.e., it is in reality $D'T$, where D' is a complex diagonal matrix with an unknown speckle pattern on its diagonal [14]. However, because the SLM acts only at the input of the medium, the presence of D' does not impact our simulations. For clarify, the measured transmission matrix is then written as T.

In this simulation, two different types of images are produced at the output for two different phase patterns programmed on the SLM. Figure 9(a) shows the sum-coordinate projection of $|\Psi_{\text{out}}|^2$ obtained with a flat phase pattern, i.e., $\theta_k = 0$ for all $k \in [\![1, 1024]\!]$. It shows a speckle pattern similar to the one observed experimentally in Fig. 2(d), albeit with a higher pixel resolution. Figure 9(b) shows the sum-coordinate projection of $|\Psi_{\text{out}}|^2$ obtained with the phase pattern $\theta_k = \arg(T^*_{pk})$, for $k \in$

[[1, 1024]], where p is the central pixel of the camera. This phase pattern is shown in Fig. 1(c). In this case, we observe the presence of a strong coincidence peak in the output sum-coordinate projection, showing that spatial correlations are restored at the output when programming this phase pattern. This corresponds to the experimental results shown in Fig. 2(f).

2. Simulations of entanglement manipulation through a thick scattering medium

In this section, we simulate the propagation and manipulation of spatially entangled photon pairs through a thick scattering medium. In such a general case, Eqs. (2) and (3) cannot be simplified and perfectly satisfied using a single SLM. Nevertheless, using an optimization approach, one can try to get as close as possible to the ideal situation. In the following example, we describe a computer-based optimization algorithm that refocuses photons pairs in coincidence in both the position and momentum basis.

Figure 10(a) shows the experimental setup associated with our simulation. Entangled photons propagating in the position and momentum-basis configurations are described by the following two equations:

$$TD_2 P_d D_1^2 P_d^t D_2 T^t = \Psi_p^{\text{out}}, \tag{H2}$$

$$FTD_2 P_d D_1^2 P_d^t D_2 T^t F^t = \Psi_m^{\text{out}}. \tag{H3}$$

D_1 and D_2 are diagonal matrices associated with SLM1 and SLM2, respectively, P_d is the matrix associated with free-space propagation over the distance d, Ψ_p^{out} and Ψ_m^{out} are the two two-photon output fields in the position- and momentum-basis configurations, respectively, and T is the transmission matrix of the scattering medium. T can be generated numerically as an independent identically distributed complex Gaussian matrix, as we do to obtain the results shown in Figs. 10(b)–10(e), or it can alternatively be measured experimentally using classical light (as in Ref. [14]) and then loaded onto the computer. To perform the optimization approach, we choose as an optimization target the sum of the coincidence rates taken at the center of the minus-coordinate projection in the position basis and the sum of the coincidence rate taken at the center of the sum-coordinate projection in the momentum basis, i.e., $P_{p,00}^- + P_{m,00}^+$. $P_{p,00}^-$ and $P_{m,00}^+$ are defined using Eqs. B3 and B5 as follows:

$$P_{p,00}^- = = \sum_{i=1}^{N_X} \sum_{j=1}^{N_Y} |\Psi_m^{\text{out}}|_{i\,j\,i\,j}^2, \tag{H4}$$

$$P_{m,00}^+ = = \sum_{i=1}^{N_X} \sum_{j=1}^{N_Y} |\Psi_p^{\text{out}}|_{-i\,-j\,i\,j}^2, \tag{H5}$$

where N_X and N_Y are the number of elements in each spatial axis used in our simulation. When performing
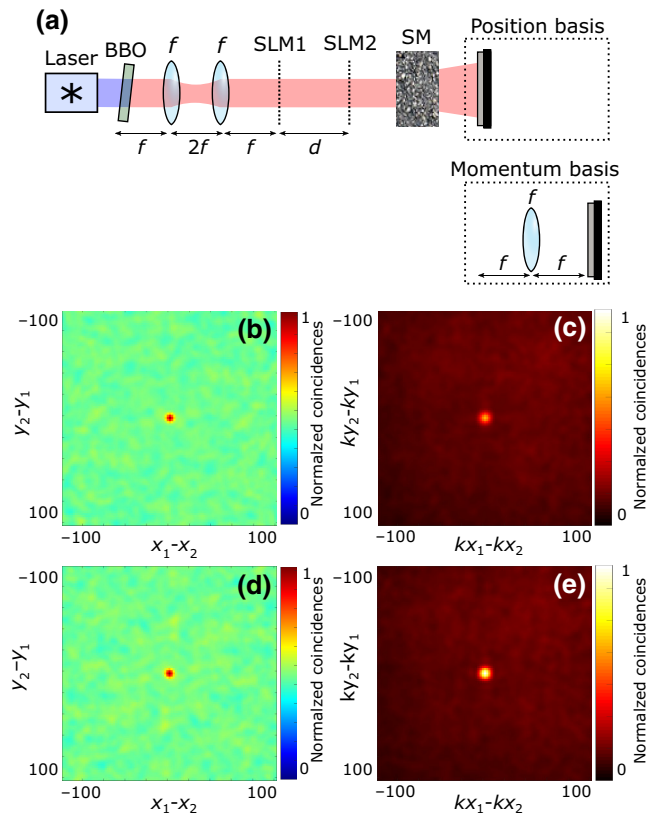

FIG. 10. The simulation of entangled photons propagating through a thick scattering medium. (a) The experimental setup considered in our simulation. The pump beam has a wavelength of 405 nm and a beam diameter of 5 mm. The focal length is $f = 500$ mm and the propagation distance $d = 200$ mm. The nonlinear crystal is considered to be infinitely thin. (b) The minus-coordinate projection measured in the position-basis configuration and (c) the sum-coordinate projection measured in the momentum-basis configuration after optimization using SLM1. (d) The minus-coordinate projection measured in the position-basis configuration and (e) the sum-coordinate projection measured in the momentum-basis configuration after optimization using SLM1 and SLM2. SM, scattering medium; SLM, spatial light modulator; BBO, β-barium borate.

the optimization using only SLM1 (i.e., SLM2 remains flat), we observe the appearance of coincidence peaks in both the minus-coordinate projection in the position basis [Fig. 10(b)] and the sum-coordinate projection in the momentum basis [Fig. 10(c)]. These results show that our optimization approach enables us to refocus entangled photons in coincidences in both bases simultaneously. To improve the refocusing process, we also insert a second SLM (SLM2) in the system at a distance d from SLM1. After optimization, Figs. 10(d) and 10(e) show an improvement in the peak-to-background ratio in both projections.

These simulation results confirm that our wavefront shaping approach can also be used to manipulate

entanglement through thick scattering media. In particular, the proposed algorithm enables us to optimize coincidences in two different output bases simultaneously, an essential step toward high-dimensional entanglement certification. In addition, we also show that using multiple SLMs (i.e., multiplane light conversion) is a promising method to achieve such a task.

3. Simulation for studying the variation of the fidelity and number of certified dimensions with the number of frames

To verify the presence of a plateau when measuring the certified dimension as a function of the number of frames (Fig. 4), we perform a simulation. For that, we use the model of the JPD dependence with the number of frames developed by Reichert *et al.* [55]. In this model, the standard deviation of a JPD coefficient Γ_{ijkl} computed from N frames scales as $\sigma_\Gamma = 1/\sqrt{N}$. Figures 12(a) and 12(b) show the simulation results obtained for two different quantum states, one maximally entangled (blue curves) and the second nonmaximally entangled (red curves). The main steps of the algorithm to obtain these results are as follows:

(1) *Generation of correlation matrices for a given N.* In the case of the maximally entangled state, a pair of correlation matrices (momentum and position) is generated using the NORMRND(MU,SIGMA) function of MATLAB. This function generates a random number from the normal distribution with mean parameter μ and standard-deviation parameter σ. Diagonal values of the two matrices are obtained using the parameters $\mu = \alpha > 0$ and $\sigma = K/\sqrt{N}$, where K is a simulation parameter and N is a parameter representing the number of frames. Off-diagonal values are obtained using parameters $\mu = 0$ and $\sigma = K/\sqrt{N}$. In the case of the nonmaximally entangled state, the only difference is that the off-diagonal elements are obtained from a random process with
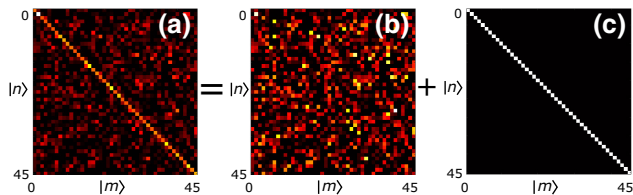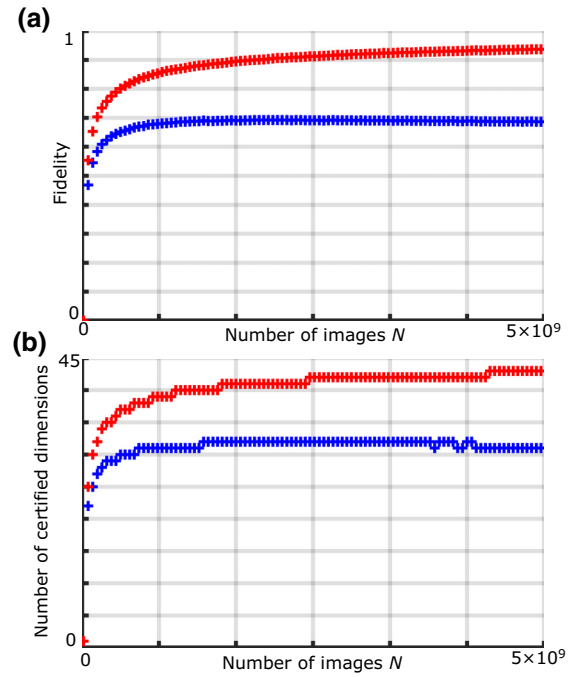

FIG. 12. The simulated fidelity and number of certified dimensions as a function of the number of frames. (a) The fidelity as a function of the number of frames N in the case of a maximally entangled state (blue) and a nonmaximally entangled state (red). (b) The number of certified dimensions as a function of the number of frames N in the case of a maximally entangled state (blue) and a nonmaximally entangled state (red). The simulations parameters are $\alpha = 1/45$, $\alpha' = 0.0001$, and $K = 1$.

a nonzero mean parameter $\mu = \alpha' < \alpha$. The matrices have dimensions 45×45. Figure 11 shows an example of the generation of one correlation matrix.

(2) *Calculation of the fidelity and the number of certified dimensions.* For a given N, a set 100 pairs of correlation matrices is generated in each case (i.e., maximally and nonmaximally entangled). The fidelity is then calculated for each pair of matrices using Eqs. (F4)–(F9) and averaged over the set. Then, Eq. (5) is used to calculate the number of certified dimensions. This process is repeated for different numbers of frames N to obtain the curves in Figs. 12(a) and 12(b).

Ther results shown in Fig. 12 confirm the presence of plateaus for large N in each case.

———

FIG. 11. The simulation of a correlation matrix. In the case of the maximally entangled state, a (a) correlation matrix is obtained by adding a (b) 45×45 matrix made of random values with mean parameter 0 and standard deviation $\sigma = 1/\sqrt{N}$, where N is the number of frames, to a (c) 45×45 diagonal matrix with diagonal values α. In this example, $N = 10^6$ and $\alpha = 1/45$.

[1] M. Mirhosseini, O. S. Magaña-Loaiza, M. N. O'Sullivan, B. Rodenburg, M. Malik, M. P. J. Lavery, M. J. Padgett, D. J. Gauthier, and R. W. Boyd, High-dimensional quantum cryptography with twisted light, New J. Phys. **17**, 033033 (2015).

[2] S. Ecker, F. Bouchard, L. Bulla, F. Brandt, O. Kohout, F. Steinlechner, R. Fickler, M. Malik, Y. Guryanova, R. Ursin, and M. Huber, Overcoming Noise in Entanglement Distribution, Phys. Rev. X **9**, 041042 (2019).

[3] A. Acín, N. Brunner, N. Gisin, S. Massar, S. Pironio, and V. Scarani, Device-Independent Security of Quantum Cryptography against Collective Attacks, Phys. Rev. Lett. **98**, 230501 (2007).

[4] G. Brida, M. Genovese, and I. R. Berchera, Experimental realization of sub-shot-noise quantum imaging, Nat. Photon. **4**, 227 (2010).

[5] E. Toninelli, P.-A. Moreau, T. Gregory, A. Mihalyi, M. Edgar, N. Radwell, and M. Padgett, Resolution-enhanced quantum imaging by centroid estimation of biphotons, Optica **6**, 347 (2019).

[6] R. Camphausen, A. Cuevas, L. Duempelmann, R. A. Terborg, E. Wajs, S. Tisa, A. Ruggeri, I. Cusini, F. Steinlechner, and V. Pruneri, and A quantum-enhanced wide-field phase imager, Sci. Adv. **7**, eabj2155 (2021).

[7] H. Defienne, P. Cameron, B. Ndagano, A. Lyons, M. Reichert, J. Zhao, A. R. Harvey, E. Charbon, J. W. Fleischer, and D. Faccio, Pixel super-resolution with spatially entangled photons, Nat. Commun. **13**, 3566 (2022).

[8] B. Ndagano, H. Defienne, D. Branford, Y. D. Shah, A. Lyons, N. Westerberg, E. M. Gauger, and D. Faccio, Quantum microscopy based on Hong-Ou-Mandel interference, Nat. Photon. **16**, 384 (2022).

[9] H. Defienne, M. Reichert, J. W. Fleischer, and D. Faccio, Quantum image distillation, Sci. Adv. **5**, eaax0307 (2019).

[10] T. Gregory, P.-A. Moreau, E. Toninelli, and M. J. Padgett, Imaging through noise with quantum illumination, Sci. Adv. **6**, eaay2652 (2020).

[11] F. Devaux, A. Mosset, F. Bassignot, and E. Lantz, Quantum holography with biphotons of high Schmidt number, Phys. Rev. A **99**, 033854 (2019).

[12] H. Defienne, B. Ndagano, A. Lyons, and D. Faccio, Polarization entanglement-enabled quantum holography, Nat. Phys. **17**, 591 (2021).

[13] I. M. Vellekoop and A. P. Mosk, Focusing coherent light through opaque strongly scattering media, Opt. Lett. **32**, 2309 (2007).

[14] S. M. Popoff, G. Lerosey, R. Carminati, M. Fink, A. C. Boccara, and S. Gigan, Measuring the Transmission Matrix in Optics: An Approach to the Study and Control of Light Propagation in Disordered Media, Phys. Rev. Lett. **104**, 100601 (2010).

[15] J. Carpenter, B. J. Eggleton, and J. Schröder, 110×110 optical mode transfer matrix inversion, Opt. Express **22**, 96 (2014).

[16] M. Plöschner, T. Tyc, and T. Čižmár, Seeing through chaos in multimode fibres, Nat. Photon. **9**, 529 (2015).

[17] S. Kang, S. Jeong, W. Choi, H. Ko, T. D. Yang, J. H. Joo, J.-S. Lee, Y.-S. Lim, Q.-H. Park, and W. Choi, Imaging deep within a scattering medium using collective accumulation of single-scattered waves, Nat. Photon. **9**, 253 (2015).

[18] A. Badon, D. Li, G. Lerosey, A. C. Boccara, M. Fink, and A. Aubry, Smart optical coherence tomography for ultra-deep imaging through highly scattering media, Sci. Adv. **2**, e1600370 (2016).

[19] J. Carpenter, C. Xiong, M. J. Collins, J. Li, T. F. Krauss, B. J. Eggleton, A. S. Clark, and J. Schröder, Mode multiplexed single-photon and classical channels in a few-mode fiber, Opt. Express **21**, 28794 (2013).

[20] T. J. Huisman, S. R. Huisman, A. P. Mosk, and P. W. H. Pinkse, Controlling single-photon Fock-state propagation through opaque scattering media, Appl. Phys. B **116**, 603 (2014).

[21] H. Defienne, M. Barbieri, B. Chalopin, B. Chatel, I. A. Walmsley, B. J. Smith, and S. Gigan, Nonclassical light manipulation in a multiple-scattering medium, Opt. Lett. **39**, 6090 (2014).

[22] H. Defienne, M. Barbieri, I. A. Walmsley, B. J. Smith, and S. Gigan, Two-photon quantum walk in a multimode fiber, Sci. Adv. **2**, e1501054 (2016).

[23] T. A. W. Wolterink, R. Uppu, G. Ctistis, W. L. Vos, K.-J. Boller, and P. W. H. Pinkse, Programmable two-photon quantum interference in 10^3 channels in opaque scattering media, Phys. Rev. A **93**, 053817 (2016).

[24] H. Defienne, M. Reichert, and J. W. Fleischer, Adaptive Quantum Optics with Spatially Entangled Photon Pairs, Phys. Rev. Lett. **121**, 233601 (2018).

[25] F. Devaux, A. Mosset, S. M. Popoff, and E. Lantz, Restoring and tailoring very high dimensional spatial entanglement of a biphoton state transmitted through a scattering medium (2022), ArXiv:2206.00299.

[26] O. Lib, G. Hasson, and Y. Bromberg, Real-time shaping of entangled photons by classical control and feedback, Sci. Adv. **6**, eabb6298 (2020).

[27] N. H. Valencia, S. Goel, W. McCutcheon, H. Defienne, and M. Malik, Unscrambling entanglement through a complex medium, Nat. Phys. **16**, 1112 (2020).

[28] N. Friis, G. Vitagliano, M. Malik, and M. Huber, Entanglement certification from theory to experiment, Nat. Rev. Phys. **1**, 72 (2019).

[29] B. Ndagano, H. Defienne, A. Lyons, I. Starshynov, F. Villa, S. Tisa, and D. Faccio, Imaging and certifying high-dimensional entanglement with a single-photon avalanche diode camera, npj Quantum Inf. **6**, 1 (2020).

[30] A. Einstein, B. Podolsky, and N. Rosen, Can quantum-mechanical description of physical reality be considered complete? Phys. Rev. **47**, 777 (1935).

[31] V. Giovannetti, S. Mancini, D. Vitali, and P. Tombesi, Characterizing the entanglement of bipartite quantum systems, Phys. Rev. A **67**, 022320 (2003).

[32] J. Bavaresco, N. H. Valencia, C. Klöckl, M. Pivoluska, P. Erker, N. Friis, M. Malik, and M. Huber, Measurements in two bases are sufficient for certifying high-dimensional entanglement, Nat. Phys. **14**, 1032 (2018).

[33] D. Bronzi, F. Villa, S. Tisa, A. Tosi, F. Zappa, D. Durini, S. Weyers, and W. Brockherde, 100 000 Frames/s 64×32 Single-Photon Detector Array for 2-D Imaging and 3-D Ranging, IEEE J. Sel. Top. Quantum Electron. **20**, 354 (2014).

[34] P. Erker, M. Krenn, and M. Huber, Quantifying high dimensional entanglement with two mutually unbiased bases, Quantum **1**, 22 (2017).

[35] J. C. Howell, R. S. Bennink, S. J. Bentley, and R. W. Boyd, Realization of the Einstein-Podolsky-Rosen Paradox Using Momentum- and Position-Entangled Photons from Spontaneous Parametric Down Conversion, Phys. Rev. Lett. **92**, 210403 (2004).

[36] P.-A. Moreau, J. Mougin-Sisini, F. Devaux, and E. Lantz, Realization of the purely spatial Einstein-Podolsky-Rosen paradox in full-field images of spontaneous parametric down-conversion, Phys. Rev. A **86**, 010101 (2012).

[37] M. P. Edgar, D. S. Tasca, F. Izdebski, R. E. Warburton, J. Leach, M. Agnew, G. S. Buller, R. W. Boyd, and M. J. Padgett, Imaging high-dimensional spatial entanglement with a camera, Nat. Commun. **3**, 984 (2012).

[38] M. Dabrowski, M. Parniak, and W. Wasilewski, Einstein-Podolsky-Rosen paradox in a hybrid bipartite system, Optica **4**, 272 (2017).

[39] H. Defienne, M. Reichert, and J. W. Fleischer, General Model of Photon-Pair Detection with an Image Sensor, Phys. Rev. Lett. **120**, 203604 (2018).

[40] M. V. Fedorov, Y. M. Mikhailova, and P. A. Volkov, Gaussian modelling and Schmidt modes of SPDC biphoton states, J. Phys. B: At., Mol. Opt. Phys. **42**, 175503 (2009).

[41] S. Gnatiessoro, A. Mosset, E. Lantz, and F. Devaux, Imaging Spatial Quantum Correlations through a thin Scattering Medium, OSA Continuum **2**, 3393 (2019).

[42] G. Soro, E. Lantz, A. Mosset, and F. Devaux, Quantum spatial correlations imaging through thick scattering media: Experiments and comparison with simulations of the biphoton wave function, J. Opt. **23**, 025201 (2021).

[43] J.-F. Morizur, L. Nicholls, P. Jian, S. Armstrong, N. Treps, B. Hage, M. Hsu, W. Bowen, J. Janousek, and H.-A. Bachor, Programmable unitary spatial mode manipulation, JOSA A **27**, 2524 (2010).

[44] N. K. Fontaine, R. Ryf, H. Chen, D. T. Neilson, K. Kim, and J. Carpenter, Laguerre-Gaussian mode sorter, Nat. Commun. **10**, 1 (2019).

[45] O. Lib, K. Sulimany, and Y. Bromberg, Processing Entangled Photons in High Dimensions with a Programmable Light Converter, Phys. Rev. Appl. **18**, 014063 (2022).

[46] F. Brandt, M. Hiekkamäki, F. Bouchard, M. Huber, and R. Fickler, High-dimensional quantum gates using full-field spatial modes of photons, Optica **7**, 98 (2020).

[47] F. Madonini, F. Severini, F. Zappa, and F. Villa, Single photon avalanche diode arrays for quantum imaging and microscopy, Adv. Quantum Technol. **4**, 2100005 (2021).

[48] A. Nomerotski, Imaging and time stamping of photons with nanosecond resolution in Timepix based optical cameras, Nucl. Instrum. Methods Phys. Res. A **937**, 26 (2019).

[49] J. Schneeloch and J. C. Howell, Introduction to the transverse spatial correlations in spontaneous parametric down-conversion through the biphoton birth zone, J. Opt. **18**, 053501 (2016).

[50] I. Rech, A. Ingargiola, R. Spinelli, I. Labanca, S. Marangoni, M. Ghioni, and S. Cova, Optical crosstalk in single photon avalanche diode arrays: A new complete model, Opt. Express **16**, 8381 (2008).

[51] P. Connolly, X. Ren, R. Henderson, and G. Buller, Hot pixel classification of single-photon avalanche diode detector arrays using a log-normal statistical distribution, Electron. Lett. **55**, 1004 (2019).

[52] B. Eckmann, B. Bessire, M. Unternährer, L. Gasparini, M. Perenzoni, and A. Stefanov, Characterization of space-momentum entangled photons with a time resolving CMOS SPAD array, Opt. Express **28**, 31553 (2020). publisher: Optical Society of America,

[53] D. S. Tasca, P. Sánchez, S. P. Walborn, and E. Rudnicki, Mutual Unbiasedness in Coarse-Grained Continuous Variables, Phys. Rev. Lett. **120**, 040403 (2018).

[54] A. F. Abouraddy, B. E. A. Saleh, A. V. Sergienko, and M. C. Teich, Entangled-photon Fourier optics, JOSA B **19**, 1174 (2002).

[55] M. Reichert, H. Defienne, and J. W. Fleischer, Optimizing the signal-to-noise ratio of biphoton distribution measurements, Phys. Rev. A **98**, 013841 (2018).